Non-iterative numerical method for laterally superresolving Fourier domain optical coherence tomography

Yoshiaki Yasuno, Jun-ichiro Sugisaka, Yusuke Sando, Yoshifumi Nakamura, Shuichi Makita, Masahide Itoh, and Toyohiko Yatagai

Computational Optics Group, Institute of Applied Physics, University of Tsukuba, Tennodai 1-1-1, Tsukuba, Ibaraki, 305-8573, Japan

yasuno@optlab2.bk.tsukuba.ac.jp

http://optics.bk.tsukuba.ac.jp/COG/

Abstract: A numerical deconvolution method to cancel lateral defocus in Fourier domain optical coherence tomography (FD-OCT) is presented. This method uses a depth-dependent lateral point spread function and some approximations to design a deconvolution filter for the cancellation of lateral defocus. Improved lateral resolutions are theoretically estimated; consequently, the effect of lateral superresolution in this method is derived. The superresolution is experimentally confirmed by a razor blade test, and an intuitive physical interpretation of this effect is presented. The razor blade test also confirms that this method enhances the signal-to-noise ratio of OCT. This method is applied to OCT images of medical samples, *in vivo* human anterior eye segments, and exhibits its potential to cancel the defocusing of practical OCT images. The validity and restrictions involved in each approximation employed to design the deconvolution filter are discussed. A chromatic and a two-dimensional extensions of this method are also described.

OCIS codes: (100.6640) Superresolution; (100.1830) Deconvolution; (110.2990) Image formation theory; (110.4500) Optical coherence tomography; (170.4500) Optical coherence tomography

References and links

1. D. Huang, E. A. Swanson, C. P. Lin, J. S. Schuman, W. G. Stinson, W. Chang, M. R. Hee, T. Flotte, K. Gregory, C. A. Puliafito, and J. G. Fujimoto, "Optical coherence tomography," Science **254,** 1178–1181 (1991).
2. W. Drexler, U. Morgner, F. X. Kartner, C. Pitris, S. A. Boppart, X. D. Li, E. P. Ippen, and J. G. Fujimoto, "*In vivo* ultrahigh-resolution optical coherence tomography," Opt. Lett. **24,** 1221–1223 (1999).
3. B. Povazay, K. Bizheva, A. Unterhuber, B. Hermann, H. Sattmann, A. F. Fercher, W. Drexler, A. Apolonski, W. J. Wadsworth, J. C. Knight, P. St. J. Russell, M. Vetterlein, and E. Scherzer, "Submicrometer axial resolution optical coherence tomography," Opt. Lett. **27,** 1800–1802 (2002).
4. A. F. Fercher, C. K. Hitzenberger, G. Kamp, and S. Y. El-Zaiat, "Measurement of intraocular distances by backscattering spectral interferometry," Opt. Commun. **117,** 43–48 (1995).
5. Gerd Häusler and Michael Walter Lindner, " 'Coherence radar' and 'spectral radar' —New tools for dermatological diagnosis," J. Biomed. Opt. **3,** 21–31 (1998).
6. P. Andretzky, M. W. Lindner, J. M. Herrmann, A. Schultz, M. Konzog, F. Kiesewetter, and G. H ausler , "Optical coherence tomography by spectral radar: dynamic range estimation and in-vivo measurements of skin," Proc. SPIE **3567,** 78–87 (1999).

#9985 - $15.00 USD Received 15 December 2005; revised 20 January 2006; accepted 23 January 2006

7. T. Mitsui, "Dynamic range of optical reflectometry with spectral interferometry," Jpn. J. Appl. Phys. **38,** 6133–6137 (1999).
8. R. A. Leitgeb, C. K. Hitzenberger, and A. F. Fercher," Performance of fourier domain vs. time domain optical coherence tomography," Opt. Express **11,** 889–894 (2003), http://www.opticsexpress.org/abstract.cfm?URI=OPEX-11-8-889.
9. J. F. de Boer, B. Cense, B. H. Park, M. C. Pierce, G. J. Tearney, and B. E. Bouma," "Improved signal-to-noise ratio in spectral-domain compared with time-domain optical coherence tomography," Opt. Lett. **28,** 2067–2069 (2003).
10. M. A. Choma, M. V. Sarunic, C. Yang, and J. A. Izatt, "Sensitivity advantage of swept source and Fourier domain optical coherence tomography," Opt. Express **11,** 2183–2189 (2003), http://www.opticsinfobase.org/abstract.cfm?URI=oe-11-18-2183.
11. S. H. Yun, G. J. Tearney, J. F. de Boer, N. Iftimia, and B. E. Bouma, "High-speed optical frequency-domain imaging," Opt. Express **11,** 2953–2963 (2003), http://www.opticsinfobase.org/abstract.cfm?URI=oe-11-22-2953.
12. N. A. Nassif, B. Cense, B. H. Park, M. C. Pierce, S. H. Yun, B. E. Bouma, G. J. Tearney, T. C. Chen, and J. F. de Boer, "*In vivo* high-resolution video-rate spectral-domain optical coherence tomography of the human retina and optic nerve," Opt. Express **12,** 367–376 (2004), http://www.opticsinfobase.org/abstract.cfm?URI=oe-12-3-367.
13. R. Huber, M. Wojtkowski, K. Taira, J. G. Fujimoto, and K. Hsu, "Amplified, frequency swept lasers for frequency domain reflectometry and OCT imaging: design and scaling principles," Opt. Express **13** 3513–3528 (2005), http://www.opticsinfobase.org/abstract.cfm?URI=oe-13-9-3513.
14. M. Wojtkowski, R. Leitgeb, A. Kowalczyk, T. Bajraszewski, and A. F. Fercher, "*In vivo* human retinal imaging by Fourier domain optical coherence tomography," J. Biomed. Opt. **7,** 457–463 (2002).
15. N. A. Nassif, B. Cense, B. H. Park, M. C. Pierce, S. H. Yun, B. E. Bouma, G. J. Tearney, T. C. Chen, and J. F. de Boer, "*In vivo* high-resolution video-rate spectral-domain optical coherence tomography of the human retina and optic nerve," Opt. Express **12,** 367–376 (2004), http://www.opticsexpress.org/abstract.cfm?URI=OPEX-12-3-367.
16. R. A. Leitgeb, W. Drexler, A. Unterhuber, B. Hermann, T. Bajraszewski, T. Le, A. Stingl, and A. F. Fercher, "Ultrahigh resolution Fourier domain optical coherence tomography," Opt. Express **12,** 2156–2165 (2004), http://www.opticsexpress.org/abstract.cfm?URI=OPEX-12-10-2156.
17. M. Wojtkowski, V. J. Srinivasan, T. H. Ko, and J. G. Fujimoto, A. Kowalczyk, and J. S. Duker, "Ultrahigh-resolution, high-speed, Fourier domain optical coherence tomography and methods for dispersion compensation," Opt. Express **12,** 2404–2422 (2004), http://www.opticsexpress.org/abstract.cfm?URI=OPEX-12-11-2404.
18. B. Cense, N. A. Nassif, T. C. Chen, M. C. Pierce, S. H. Yun, B. H. Park, B. E. Bouma, G. J. Tearney, and J. F. de Boer, "Ultrahigh-resolution high-speed retinal imaging using spectral-domain optical coherence tomography," Opt. Express **12,** 2435–2447 (2004), http://www.opticsexpress.org/abstract.cfm?URI=OPEX-12-11-2435.
19. S. Jiao, R. Knighton, X. Huang, G. Gregori, and C. A. Puliafito, "Simultaneous acquisition of sectional and fundus ophthalmic images with spectral-domain optical coherence tomography," Opt. Express **12,** 444–452 (2005), http://www.opticsexpress.org/abstract.cfm?URI=OPEX-13-2-444.
20. M. Wojtkowski, V. Srinivasan, J. G. Fujimoto, T. Ko, J. S. Schuman, A. Kowalczyk, and J. S. Duker, "Three-dimensional retinal imaging with high-speed ultrahigh-resolution optical coherence tomography," Ophthalmology **112,** 1734–1746 (2005).
21. Z. P. Chen, T. E. Milner, S. Srinivas, X. Wang, A. Malekafzali, M. J. C. van Gemert, and J. S. Nelson, "Noninvasive imagingof *in vivo* blood flow velocity usingoptical Doppler tomography," Opt. Lett. **22,** 1119–1121 (1997).
22. Y. Zhao, Z. Chen, C. Saxer, S. Xiang, J. de Boer, and J. Nelson, "Phase-resolved optical coherence tomography and optical Doppler tomography for imaging blood f low in human skin with fast scanning speed and high velocity sensitivity," Opt. Lett. **25,** 114–116 (2000).
23. Y. Yasuno, S. Makita, Y. Sutoh, M. Itoh, and T. Yatagai, "Birefringence imaging of human skin by polarization-sensitive spectral interferometric optical coherence tomography," Opt. Lett. **27,** 1803–1805 (2002).
24. Y. Yasuno, S. Makita, T. Endo, M. Itoh, T. Yatagai, M. Takahashi, C. Katada, and M. Mutoh, "Polarization-sensitive complex Fourier domain optical coherence tomography for Jones matrix imaging of biological samples," Appl. Phys. Lett. **85,** 3023–3025 (2004).
25. J. Zhang, W. Jung, J. S. Nelson, and Z. P. Chen, "Full range polarization-sensitive Fourier domain optical coherence tomography," Opt. Express **12,** 6033–6039 (2004), http://www.opticsexpress.org/abstract.cfm?URI=OPEX-12-24-6033.
26. B. Park, M. Pierce, B. Cense, S. Yun, M. Mujat, G. Tearney, B. Bouma, and J. de Boer, "Real-time fiber-based multi-functional spectral-domain optical coherence tomography at 1.3 μm," Opt. Express **13,** 3931–3944 (2005), http://www.opticsexpress.org/abstract.cfm?URI=OPEX-13-11-3931.
27. R. A. Leitgeb, L. Schmetterer, W. Drexler, A. F. Fercher, R. J. Zawadzki, and T. Bajraszewski, "Real-time assessment of retinal blood flow with ultrafast acquisition by color Doppler Fourier domain optical coherence tomography," Opt. Express **11,** 3116–3121 (2003), http://www.opticsexpress.org/abstract.cfm?URI=OPEX-11-23-3116.
28. B. R. White, M. C. Pierce, N. Nassif, B. Cense, B. H. Park, G. J. Tearney, B. E. Bouma, T. C. Chen, and J. F. de Boer, "*In vivo* dynamic human retinal blood flow imaging using ultra-

#9985 - $15.00 USD Received 15 December 2005; revised 20 January 2006; accepted 23 January 2006

high-speed spectral domain optical coherence tomography," Opt. Express **11,** 3490-3497 (2003), http://www.opticsexpress.org/abstract.cfm?URI=OPEX-11-25-3490.
29. R. A. Leitgeb, L. Schmetterer, C. K. Hitzenberger, A. F. Fercher, F. Berisha, M. Wojtkowski, and T. Bajraszewski, "Real-time measurement of in vitro flow by Fourier-domain color Doppler optical coherence tomography," Opt. Lett. **29,** 171–173 (2004).
30. L. Wang, Y. Wang, S. Guo, J. Zhang, M. Bachman, G.P. Li, and Z. P. Chen, "Frequency domain phase-resolved optical Doppler and Deppler variance tomography," Opt. Commun. **242,** 345–350 (2005).
31. J. Zhang, and Z. Chen, "In vivo blood flow imaging by a swept laser source based Fourier domain optical Doppler tomography," Opt. Express **13,** 7449–7457 (2005), http://www.opticsexpress.org/abstract.cfm?URI=OPEX-13-19-7449.
32. M. A. Choma, A. K. Ellerbee, C. Yang, T. L. Creazzo, and J. A. Izatt, "Spectral-domain phase microscopy," Opt. Lett. **30,** 1162–1164 (2005).
33. C. Joo, T. Akkin, B. Cense, B. Park, and J. de Boer, "Spectral-domain optical coherence phase microscopy for quantitative phase-contrast imaging," Opt. Lett. **30,** 2131–2133 (2005).
34. Y. Zhang, J. Rha, R. Jonnal, and D. Miller, "Adaptive optics parallel spectral domain optical coherence tomography for imaging the living retina," Opt. Express **13,** 4792–4811 (2005), http://www.opticsexpress.org/abstract.cfm?URI=OPEX-13-12-4792.
35. R. Zawadzki, S. Jones, S. Olivier, M. Zhao, B. Bower, J. Izatt, S. Choi, S. Laut, and J. Werner, "Adaptive-optics optical coherence tomography for high-resolution and high-speed 3D retinal in vivo imaging," Opt. Express **13,** 8532–8546 (2005), http://www.opticsexpress.org/abstract.cfm?URI=OPEX-13-21-8532.
36. M. D. Kulkarni,C. W. Thomas, and J. A. Izatt, "Image enhancement in optical coherence tomography using deconvolution," Electron. Lett. **33** 1365–1367 (1997).
37. J. M. Schmitt, "Restoration of optical coherence images of living tissue using the clean algorithm," J. Biomed. Opt. **3,** 66–75 (1998).
38. D. Piao, Q. Zhu, N. Dutta, S. Yan, and L. Otis, "Cancellation of coherent artifacts in optical coherence tomography imaging," Appl. Opt. **40,** 5124–5131 (2001).
39. I. J. Hsu, C. W. Sun, C. W. Lu, C. C. Yang, C. P. Chiang, and C. W. Lin, "Resolution improvement with dispersion manipulation and a retrieval algorithm in optical coherence tomography," Appl. Opt. **42,** 227–234 (2003).
40. M. Bashkansky, M.D. Duncan, J. Reintjes, and P.R. Battle, "Signal processing for improving field cross-correlation function in optical coherence tomography," Appl. Opt. **37,** 8137–8138 (1998).
41. R. Tripathi, N. Nassif, J. Nelson, B. Park, and J. de Boer, "Spectral shaping for non-Gaussian source spectra in optical coherence tomography," Opt. Lett. **27,** 406–408 (2002).
42. M. Szkulmowski, M. Wojtkowski, T. Bajraszewski, I. Gorczyńska, P. Targowski, W. Wasilewski, A. Kowalczyk, and C. Radzewicz, "Quality improvement for high resolution in vivo images by spectral domain optical coherence tomography with supercontinuum source," Opt. Commun. **246,** 569–578 (2004).
43. E.g., James G. Fujimoto, "Handbook of optical coherence tomography," Chapter 1, Edited by G.R. Bouma, G.J. Tearney, Marcel Dekker, Inc. (2002).
44. D. J Smithies, T. Lindmo, Z. P. Chen, J. S. Nelson, and T. E. Milner, "Signal attenuation and localization in optical coherence tomography studied by Monte Carlo simulation," Phys. Med. Biol. **43,** 3025–3044 (1998).
45. C. Dorrer, N. Belabas, J. Likforman, and M. Joffre, "Spectral resolution and sampling issues in Fourier-transform spectral interferometry," J. Opt. Soc. Am. B **17,** 1795–1802 (2000).
46. E.g., J. W. Goodman, "Introduction to Fourier optics," 2nd ed., The McGraw-Hill Companies, Inc. (1996).

1. Introduction

Optical coherence tomography (OCT) has been widely studied since its invention [1], and applied to various aspects of biomedical tomography. One major research interest in OCT is its depth resolution; it is inversely proportional to the bandwidth of the light source. With extremely broadband light sources, microscopic OCT, namely, an optical coherence microscope that has a depth resolution of few micrometers [2] or sub-micrometers [3], has been demonstrated.

Another major topic of research in OCT is Fourier/spectral domain OCT (FD/SD-OCT) [4, 5]. FD-OCT employs a wavelength-resolving detection scheme for depth discrimination, while TD-OCT employs a mechanical-delay-based scheme. This detection scheme enables a higher sensitivity [6–11] and faster measurement speed [12, 13] than those obtained by using time-domain OCT (TD-OCT). Because of these advantages, FD-OCT is a good alternative to TD-OCT and has been widely applied to ophthalmology [14–20]; it may also have great potential in other applications. Another advantage of FD-OCT over TD-OCT is its accessibility to the

#9985 - $15.00 USD Received 15 December 2005; revised 20 January 2006; accepted 23 January 2006

phase of an OCT image. An FD-OCT image comprises complex signals, thus the amplitude and phase of the image are available, while relatively elaborate schemes or algorithms are required to obtain the phase of TD-OCT image [21,22]. Polarization sensitive FD-OCT [23–26], Doppler FD-OCT [26–31], and phase microscopy [32, 33] are examples of a phase sensitive FD-OCT.

In recent years, OCT with high lateral resolution revealed microscopic structures in biomedical samples [33–35] and has attracted much attention. If aberrations are negligible, the lateral resolution of OCT, including TD-OCT and FD-OCT, is dominated by the effective numerical aperture (NA) of an objective, which is determined by the diameter of a probe beam and the focal length of the objective, while its depth resolution is dominated by the bandwidth of the light source. Although a higher effective NA enhances lateral resolution, it narrows the depth-of-focus (DOF) in OCT. A narrow DOF reduces the depth range of measurement, and the OCT image in the out-of-focus (OOF) range is blurred laterally. Deconvolution by using a lateral point spread function (PSF) of OCT may correct the defocus and enhances the depth measurement range. Although a few deconvolution algorithms have been demonstrated for TD-OCT [36–39], most of them are nonlinear and iterative and do not use the phase of the OCT image because the phase of TD-OCT images is not available.

Spectral-shaping based deconvolution methods have also been demonstrated with TD-OCT [40, 41] and FD-OCT [42], however, these methods are of axial deconvolution.

In contrast to TD-OCT, FD-OCT provides a complex OCT, hence, it is possible to employ a complex-PSF-based deconvolution technique. In this paper, we demonstrate a phase deconvolution method for FD-OCT. This method is a lateral-oriented and non-iterative linear deconvolution method and manipulates the spatial frequency components of a complex OCT image. This method enhances the signal power, but not the noise power, further, it improves the lateral resolution over the transform-limited resolution (superresolution). The design of the spatial frequency filter for deconvolution, experimental validation of superresolution, and an example of *in vivo* measurement are shown. A few limitations of this method that takes into account the approximations employed in the designing process of the deconvolution filter, and some possible extensions of this method are discussed.

2. Methods

2.1. Lateral point spread function of OCT

The $1/e^2$-lateral resolution of OCT is expressed as [43]

$$\Delta x = 4\frac{\lambda}{\pi}\left(\frac{f}{d}\right) \tag{1}$$

where λ denotes the center wavelength of a light source, f the focal length of an objective, and d the $1/e^2$-diameter of a probe beam. It is evident that the lateral resolution improves as d/f ($\sim$2NA) becomes large. On the other hand, the depth measurement range, namely DOF, decreases with the second power of d/f as

$$\mathrm{DOF} = 8\frac{\lambda}{\pi}\left(\frac{f}{d}\right)^2 \tag{2}$$

where the DOF corresponds to the twice the Rayleigh range [43]. In the OOF range, the lateral resolution decreases due to defocusing. Hence, a high lateral resolution and wide depth measurement range are always exclusive. The method described in this paper numerically corrects the defocus in the OOF range. Since this method eliminates the above-mentioned tradeoff, it simultaneously enables a high lateral resolution and a wide DOF.

#9985 - $15.00 USD Received 15 December 2005; revised 20 January 2006; accepted 23 January 2006

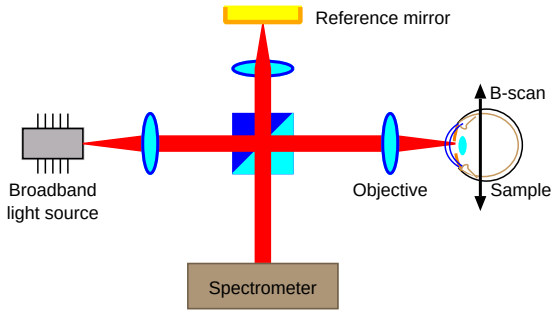

Fig. 1. Schematic of the FD-OCT under consideration; this is based on a broadband Michelson interferometer.

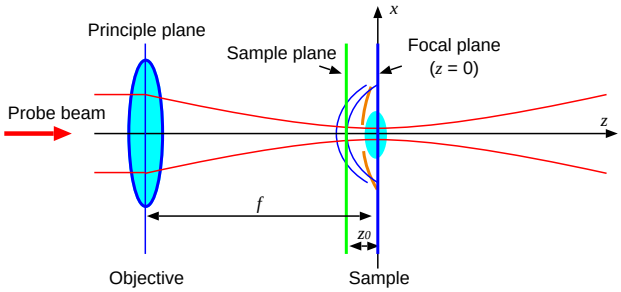

Fig. 2. Schematic diagram of probe optics. $z = 0$ on the focal plane, and z takes positive values on the right-hand-side of the focal plane.

For simplicity, an ideal free-space Michelson FD-OCT setup, as shown in Fig. 1, is considered to design a spatial frequency filter for the deconvolution method (deconvolution filter). Coordinates and notations around a focal plane and a sample plane are defined in Fig. 2.

The lateral electric field distribution on the back-focal-plane of the objective is the Fourier transform of that on the front-focal-plane;

$$u(x) \propto \mathscr{F}\left[\exp\left(-\pi\alpha x^2\right)\right]_{\xi=x/\lambda f} \propto \exp\left(-\pi\frac{x^2}{\alpha\lambda^2 f^2}\right) \tag{3}$$

where $\mathscr{F}[\,]$ represents the Fourier transform, x and ξ respectively denote the lateral position and its Fourier conjugate, i.e., the spatial frequency, $\exp\left(-\pi\alpha x^2\right)$ represents the field distribution on the front-focal-plane and $\alpha \equiv 4/\pi d^2$ is a constant defined by the $1/e^2$-diameter of the Gaussian probe beam; d.

The probe field on the sample plane ($z = z_0$) is calculated as the Fresnel diffraction of Eq. (3) with a propagation length of $-z_0$;

$$p(x,z_0) \propto \exp\left(-\pi\frac{\alpha\lambda^2 f^2}{\alpha^2\lambda^4 f^4 + \lambda^2 z_0^2}x^2\right)\exp\left(i\pi\frac{\lambda z_0}{\alpha^2\lambda^4 f^4 + \lambda^2 z_0^2}x^2\right). \tag{4}$$

The back scattered field on the sample plane becomes $p(x,z_0)f(x,z_0)$ where $f(x,z_0)$ represents the back scattering distribution, or optical structure of the sample on the sample plane.

OCT detects only the back scattered light that is scattered in the same direction as the incident light because of the confocality of the OCT detection. Hence, the probe light suffers the same

#9985 - $15.00 USD Received 15 December 2005; revised 20 January 2006; accepted 23 January 2006

phase delay as the illumination described by Eq. (4). This can be expressed as

$$q(x,z_0) = \exp\left(i\pi \frac{\lambda z_0}{\alpha^2\lambda^4 f^4 + \lambda^2 z_0^2} x^2\right). \tag{5}$$

Although snake photons originated from multiple scattering in a turbid media, such as a biological sample, could corrupt this coincidence of the phase, it is known that only ballistic and quasi-ballistic photons contribute to OCT imaging because of coherence gating [44]. Hence, it is reasonable to assume that this phase coincidence is valid not only for a specular sample but also for a biological sample.

Hence, the detected signal at $x = 0$ is expressed as

$$c(0,z_0) = \int p(x',z_0) f(x',z_0) q(x',z_0)\, dx'. \tag{6}$$

Taking into account the lateral (x) scan, this equation can be rewritten as

$$c(x,z_0) = \int p(x'-x,z_0) f(x',z_0) q(x'-x,z_0)\, dx' = \{p(x,z_0)q(x,z_0)\} * f(x,z_0) \tag{7}$$

where we used the fact that $p(x,z_0)$ and $q(x,z_0)$ are even functions and $*$ denotes the convolution operator over x. From this equation, it is evident that the PSF of this OCT detection is

$$h(x,z_0) = p(x,z_0)q(x,z_0) = \exp\left(-\pi \frac{\alpha\lambda^2 f^2}{\alpha^2\lambda^4 f^4 + \lambda^2 z_0^2} x^2\right) \exp\left(i2\pi \frac{\lambda z_0}{\alpha^2\lambda^4 f^4 + \lambda^2 z_0^2} x^2\right). \tag{8}$$

According to this equation, the PSF of the OCT detection is a complex function and comprises of not only amplitude but also phase. An FD-OCT image also comprises amplitude and phase, hence, a complex or phase deconvolution filter designed from the PSF is applicable in this case. In the following sections, the designing process of the phase deconvolution filter is described.

2.2. Design of deconvolution filter

The simplest deconvolution filter could be the inverse of the Fourier transform of Eq. (8) (See appendix A for the details of the Fourier transform.);

$$H^{-1}(\xi) \propto \exp\left(\pi \frac{a}{a^2+b^2}\xi^2\right) \exp\left(i\pi \frac{b}{a^2+b^2}\xi^2\right) \tag{9}$$

where $a = \alpha\lambda^2 f^2 / \left(\alpha^2\lambda^4 f^4 + \lambda^2 z_0^2\right)$ and $b = 2\lambda z_0 / \left(\alpha^2\lambda^4 f^4 + \lambda^2 z_0^2\right)$. However, it is evident that the amplitude of this deconvolution filter tends to infinity and enhances the noise energy as the spatial frequency ξ increases. To avoid this problem, we introduced the first approximation; we set the amplitude of this deconvolution filter to a constant, 1. Since only the relative profile of this function is important, the conservation of the signal energy was reasonably ignored to simplify the equation.

The phase of the second term of this equation also tends to infinity when $z_0 \to 0$ (see appendix B). To deal with this problem, the second approximation

$$\alpha^2\lambda^4 f^4 \ll \lambda^2 z_0^2 \tag{10}$$

is introduced. This approximation can be rewritten as

$$|z_0| \gg \frac{4\lambda}{\pi}\left(\frac{f}{d}\right)^2 = \frac{1}{2}\mathrm{DOF} \tag{11}$$

#9985 - $15.00 USD Received 15 December 2005; revised 20 January 2006; accepted 23 January 2006

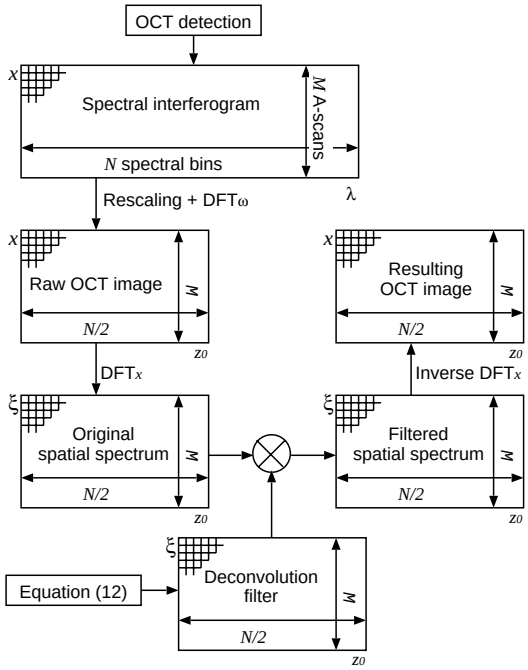

Fig. 3. Flow diagram of an algorithm to apply the deconvolution filter to detected spectral interferograms. N denotes the number of A-scans/B-scan, M denotes the number of wavelength bins, and DFT_x and DFT_k represent the discrete Fourier transform along space x and optical frequency k, respectively.

where the $\mathrm{DOF} = (8\lambda/\pi)(f/d)^2$, as determined in Eq. (2), hence, this approximation is at least valid in the OOF range. The validity in the DOF range will be demonstrated in the following sections.

According to these approximations, the deconvolution filter is simplified as follows;

$$H'^{-1}(\xi) = \exp\left(i\pi\frac{\lambda z_0}{2}\xi^2\right). \tag{12}$$

2.3. Deconvolution of the OCT image

Figure 3 shows the flow diagram to apply the above-mentioned deconvolution filter to a spectral interferogram detected by FD-OCT. In this figure, N denotes the number of A-scans for a B-scan and M denotes the number of wavelength bins in a digitized spectral interferogram. To apply this deconvolution method to an OCT image, a conventional two-dimensional complex FD-OCT image is first calculated from a two-dimensional spectral interferogram [4, 12, 14]. In the deconvolution process, discrete Fourier transform (DFT) or fast Fourier transform (FFT) is performed on each lateral line of the complex OCT image, and the DFT spectrum of the lateral line is multiplied by the inverse filter described in Eq. (12). The filtered DFT spectra are then inverse-DFTed to the original domain in order to construct a deconvolved OCT image.

#9985 - $15.00 USD Received 15 December 2005; revised 20 January 2006; accepted 23 January 2006

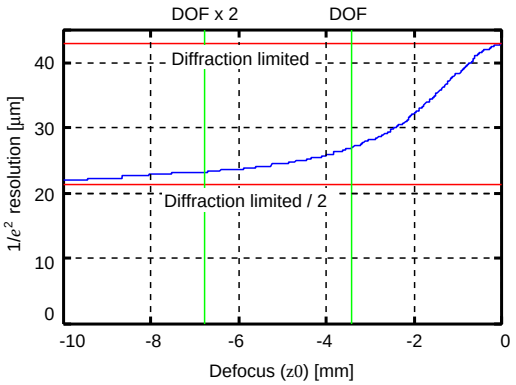

Fig. 4. Theoretical resolution curve based on Eq. (13). The considered optical parameters are d = 1.5 mm, f = 60 mm, and λ = 838 nm.

2.4. Improved lateral resolution

By applying Eq. (12) to Eq. (8), the improved lateral resolution is estimated as

$$\Delta x'(z_0) = 2\sqrt{\frac{1}{\pi}\left[\gamma\alpha\lambda^2 f^2 + \frac{z_0^2(1/2-2\gamma)^2}{\alpha f^2 \gamma}\right]} \tag{13}$$

where $\gamma = \left(\alpha^2\lambda^2 f^4 + z_0^2\right) / \left(\alpha^2\lambda^2 f^4 + 4z_0^2\right)$. Now, the lateral resolution is no longer a constant but a function of z_0. When $z_0 = 0$, this improved lateral resolution is identical to the in-focus resolution. Figure 4 shows a viewgraph of this equation. According to this viewgraph, we can conclude that the above-mentioned second approximation is acceptable not only in the OOF range but also in the DOF range. Additionally, this equation suggests an interesting property of this deconvolution method. As shown in Eq. (13) and Fig. 4, the lateral resolution approaches $\Delta x/2$, i.e., one half of the original in-focus resolution as z_0 approaches $\pm\infty$. This property predicts the lateral superresolution of this deconvolution method and is experimentally validated in the following section.

3. Experimental validations

3.1. FD-OCT setup

To experimentally validate this method, we built a standard fiber-based Michelson FD-OCT. The light source is a pigtail superluminescent diode (SLD 371HP, Superlum Diodes Ltd., Russia) with a center wavelength of 838 nm and a bandwidth of 50 nm, which results in a depth resolution of 6.2 μm in air. This light is introduced into a fiber Michelson interferometer, and 20% of the beam illuminates the sample via an objective with a focal length of 60 mm while the rest is used as a reference beam. The reference beam and 80% of the back scattered light from the sample is corrected and introduced into a spectrometer comprising of a volume holographic grating (Wasatch Photonics, UT, USA) with a groove density of 1200 lp/mm, an achromatic doublet lens (Thorlabs, Inc.) with a focal length of 200 mm, and a high-speed line CCD camera (L103k-2k, Basler Vision Technologies, Germany) with 2048 pixels and a line rate of 18.7 KHz. The digital output from the CCD camera, i.e., a spectral interferogram, is transferred to a computer via CameraLink frame grabber (mvTITAN-CL, MATRIX VISION GmbH, Germany). The spectral interferogram is rescaled from the λ-domain to k-domain by zero-filling interpolation [12, 45] and DFTed before it forms a single complex A-scan. A synchronously driven

#9985 - $15.00 USD Received 15 December 2005; revised 20 January 2006; accepted 23 January 2006

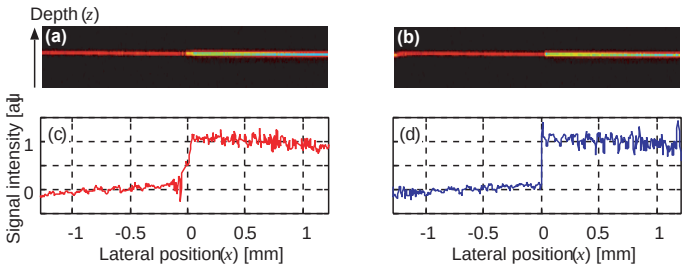

Fig. 5. (a) A raw OCT image obtained from the razor blade test and (b) an improved OCT image obtained by the deconvolution method. Intensity profiles of the surface; (c) corresponds to (a) and (d) corresponds to (b).

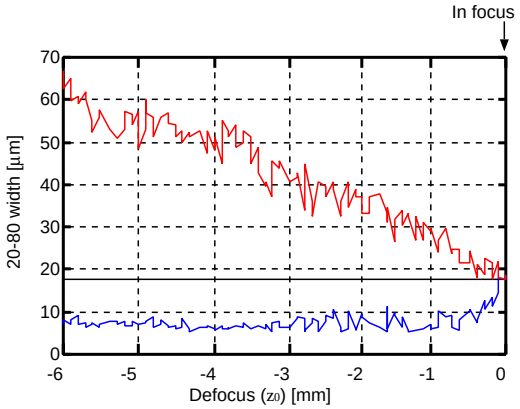

Fig. 6. The original (red curve) and improved (blue curve) 20-80 width of the razor blade test. The black solid line represents the in-focus 20-80 width.

galvano mirror (Model 6220, Cambridge Technology) in the sample arm provides a complex B-scan OCT image.

The maximum system sensitivity is measured as 101 dB in an experiment with -37 dB partial reflection mirror and 750 μW probe power, while the shot noise limited sensitivity is 107 dB. A CCD quantum efficiency of 50% and a grating diffraction efficiency of 80% are used to calculate the shot noise limited sensitivity.

3.2. Razor blade test

A razor blade test is employed to examine lateral resolutions. The measured sample is a test target, which is a glass plate where half the sample is aluminum-coated. The edge between the glass and aluminum is measured by OCT. An OCT image of this razor blade test with 4 mm defocus is shown in Fig. 5(a). Figure 5(b) shows the same OCT image but with deconvolution. Figures 5(c) and 5(d) represent corresponding one-dimensional intensity profiles of the surface of Figs. 5(a) and 5(b). According to these figures, it is evident that the lateral resolution is improved by this deconvolution. We see a noise spike on the edge of Fig. 5(d). Although this noise seems like an overshooting spike, it is not the overshooting spike but a conventional image noise because it is not visible in other measurements.

To quantify this examination, the intensity profiles of this surface of the sample is fitted by

#9985 - $15.00 USD Received 15 December 2005; revised 20 January 2006; accepted 23 January 2006

the sigmoidal curve;

$$s(x) = \frac{1}{1 + e^{-\eta(x-\varepsilon)}} \tag{14}$$

where η and ε are fitting coefficients that correspond to the steepness and the center position of the sigmoidal curve respectively. Consequently, the full width of 20% and 80% maximum (20-80 width) of the curve is determined from η and is used as a measure of lateral resolution. Figure 6 plots the 20-80 widths over defocus z_0. The red curve corresponds to the 20-80 width of the raw OCT images and the blue curve corresponds to that of the deconvolved OCT images. Here, it is evident that the 20-80 width of the OOF range is twice as better as that of the in-focus. This plot experimentally proves superresolution in the OOF range.

When z_0 = 0, the 20-80 width (Δx_{20-80}) is related to $1/e^2$-width (Δx) by the equation;

$$\Delta x_{20-80} = \sqrt{\ln 2 \cdot \ln \frac{5}{4}}\, \Delta x. \tag{15}$$

According to this equation, the theoretical in-focus 20-80 width is 17 μm with our optical parameters of d = 1.5 mm and f = 60 mm, and it is agreed with the experiment. In the OOF range, the relationship between the 20-80 width and the $1/e^2$-width is too elaborate to obtain analytically. However, the razor blade test is one of the standard tests for lateral resolution of in-focus imaging. Since the improved $1/e^2$-resolution can not be measured directly, the 20-80 width of the razor blade test may be a reasonable measure of the lateral resolution.

3.3. Physical interpretation of superresolution

Although superresolution is evident from Eq. (13), we may provide some physical and intuitive interpretations of this effect. In the OOF range, the wavefront of a probe beam has a spherical shape whose center is the focal point of an objective. This spherical wavefront illuminates the sample and is scattered back along the incident direction. In this backpropagation process, the curvature of the spherical wavefront doubles as shown in Eq. (8). Because of this twofold curvature of the probe beam, the effective NA of the objective is virtually doubled. If the deconvolution method is not employed, the lateral resolution decreases because the twofold curvature induces defocusing. However, since the defocusing is canceled by deconvolution, the twofold NA improves the lateral resolution.

On the other hand, in the DOF rage, the wavefront is regarded as a plane wavefront, and the twofold curvature is not evident. Hence, superresolution is not evident in this range, and it agrees with Figs. 4 and 6 and Eq. (13). The difference in the shape of the wavefronts between these two ranges also corresponds to an implicit approximation of the Fresnel diffraction, which is discussed later in section 4.2.

3.4. SNR enhancement

It was also found that our phase-only deconvolution filter enhanced the signal-to-noise ratio (SNR) of OCT, whereas most of the intensity deconvolution filters decrease the SNR. The following description may explain this improvement in SNR. The phase of the OCT signal is distorted systematically in a spatial frequency domain by defocusing. This systematic distortion can be canceled by the phase deconvolution filter, hence, the signal concentration in space domain increases, and the signal has a higher peak amplitude than that without deconvolution. Consequently, the signal energy, which is the summation of the squared amplitude of the signal of each OCT pixel, increases.

On the other hand, the phase of noise is random both before and after the deconvolution. Hence, there is a constant noise distribution in the space domain both with and without the

#9985 - $15.00 USD Received 15 December 2005; revised 20 January 2006; accepted 23 January 2006

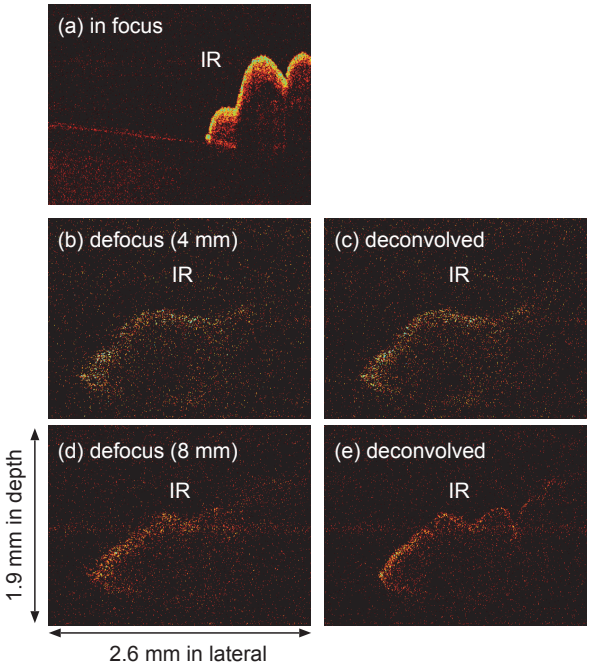

Fig. 7. FD-OCT images of *in vivo* human anterior eye segments. (a) is an in-focus OCT image, (b) and (d) are OCT images with 4-mm and 8-mm defocus, and (c) and (e) are OCT images with deconvolution. IR denotes the iris and CL denotes the crystalline lens.

deconvolution. Consequently, the noise energy after deconvolution is identical to that before deconvolution. Finally, the ratio of these two energies, namely, SNR, increases.

Although 1 dB improvement of SNR was confirmed in the above-mentioned razor blade test, further investigation is needed to proof the SNR enhancement experimentally.

3.5. Measurement of biological sample

To demonstrate the applicability of the deconvolution method to biological samples, we apply this method to *in vivo* OCT measurement of human anterior eye segments. The investigation of anterior eye segments is one of the applications of OCT that requires a large depth-measurement range where a short DOF range is problematic. Figure 7(a) shows an example of an in-focus OCT of a human anterior eye segment. Here, the surface of the crystalline lens and iris stroma are evident. Figure 7(b) shows an OCT image of the same sample with 4-mm defocusing, and Fig. 7(c) shows the same image after deconvolution. This effect is also evident in Figs. 7(d) and 7(e), in which the defocus length is 8 mm. The faint structures on the surface of the iris in Figs. 7(d) are clearly improved and easily recognized in Fig. 7(e). Here, it should be noted that the drop in SNR in Figs. 7(c) and 7(e) is caused by the confocality of the fiber interferometer. The confocal parameter of this setup is 1.9 mm, and is relatively smaller than the defocus length.

The image quality of Fig. 7(c) is worse than that of Fig. 7(e) despite its shorter defocus length. A phase error due to sample motion may account for this contradiction. Because our deconvolution method is a phase sensitive method, the phase error from the sample motion suppresses the performance of the deconvolution. Further improvement of the measurement speed of FD-OCT will overcome this problem.

#9985 - $15.00 USD Received 15 December 2005; revised 20 January 2006; accepted 23 January 2006

4. Discussions

4.1. Limitation of the NA of an objective

In Eq. (3), the field distribution on the back-focal-plane of the objective is considered as the Fourier transform of the field distribution on the front-focal-plane. This Fourier transform relies on lens-induced Fraunhofer diffraction, which in turn relies on Fresnel diffraction. Therefore, the Fresnel diffraction integral was employed to calculate the diffraction from the principle plane of the objective to the back-focal-plane. Hence, the beam diameter d and focal length of the objective f should satisfy the criterion of Fresnel diffraction [46]

$$l_z^3 > \frac{\pi}{4\lambda}\left[\left(\frac{W_x + W_x'}{2}\right)^4\right]_{\max} \tag{16}$$

where l_z denotes the propagation length, and W_x and W_x' denote the lateral extensions of electric fields on the source and destination planes of the diffraction, respectively.

Since, in our case, l_z corresponds to the focal length of the objective f, the probe beam diameter d can be regarded as W_x, and the condition becomes

$$f > \left[\frac{\pi}{4\lambda}\left(\frac{d}{2}\right)^4\right]^{1/3} \tag{17}$$

where we assume that the spot size of the probe beam on a sample plane W_x' is much smaller than the beam diameter d.

With the parameters of our experiment, d = 1.5 mm and λ = 838 nm, the above condition becomes $f > 6.7$ mm; our setup satisfies this condition. This condition can also be written in other forms, e.g., an effective NA < 0.11 or $d/f < 0.22$; this condition is satisfactory for most OCT systems. Another description of this condition is that the virtually doubled NA (described in section 3.3) can not exceed 0.22 with the above-mentioned experimental parameters.

4.2. Limitation of the superresolution range

The defocused probe field on the sample plane $p(x, z_0)$ (Eq. (4)) was derived from the field distribution of the back-focal-plane (Eq. (3)) by Fresnel diffraction. This Fresnel diffraction imposes the following condition on the propagation length z_0 by Eq. (16);

$$|z_0| > \left(\frac{\lambda}{\pi}\mathrm{DOF}^2\right)^{1/3} \tag{18}$$

where we assume $W_x = W_x' = \Delta x$. The experimental parameters of λ = 838 nm, f = 60 mm, and d = 1.5 mm yield the condition $|z_0| > 67\ \mu$m.

However, as mentioned in section 2.2, the approximation employed to design the filter (Eq. (10)) results in another condition (Eq. (11)). With the above-mentioned parameters, this condition becomes $|z_0| \gg 780\ \mu$m. Since this condition is stricter than Eq. (18), Eq. (11) determines the minimum defocus length for the approximations.

In practice, when the above-mentioned conditions are not satisfied, the effect of superresolution is not entirely clear. This limitation of superresolution is evident from Eq. (13) and in Fig. 6.

4.3. Monochromatic versus chromatic algorithms

An implicit approximation has been employed in this method. In the previous sections, the wavelength λ was regarded as a constant and we typically used the center wavelength of the broadband light source as λ (monochromatic approximation).

#9985 - $15.00 USD Received 15 December 2005; revised 20 January 2006; accepted 23 January 2006

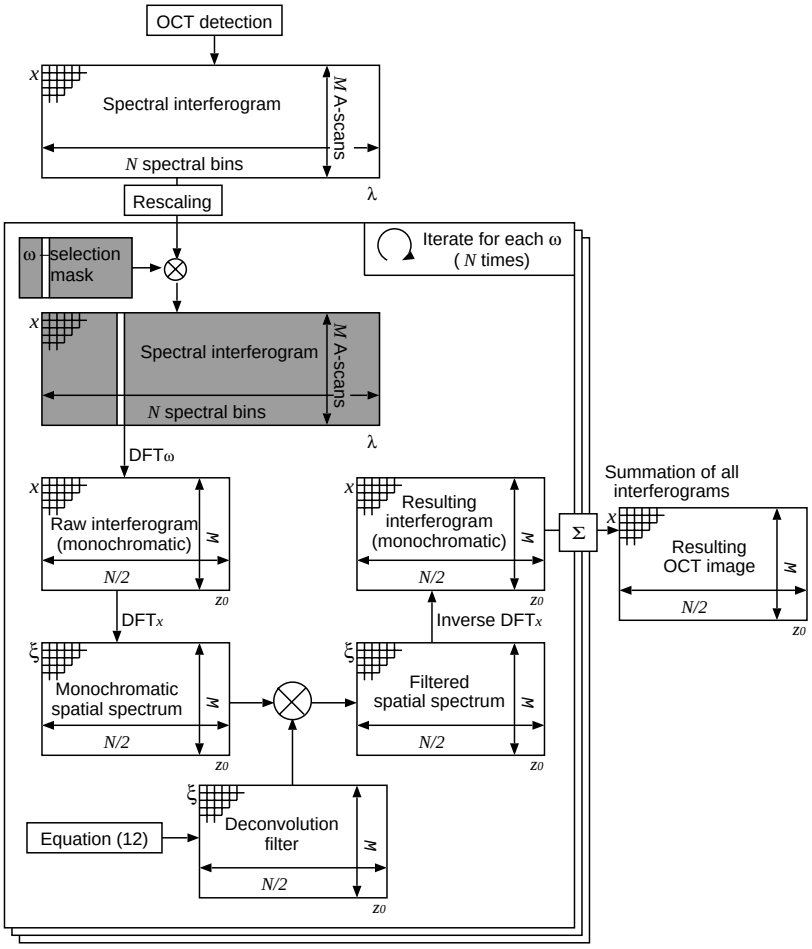

Fig. 8. Flow of the chromatic algorithm.

In reality, the light source of OCT is broadband with an extension in the wavelength. Because FD-OCT detects a wavelength-resolved spectral interferogram, the algorithm may be modified to take into account this broadening of the spectrum by using straightforward method, i.e., we could design deconvolution filters for several wavelengths and apply them to each wavelength component as shown in Fig. 8.

Although the concept of a chromatic algorithm is not elaborate, it is expensive with regard to the calculation time. This chromatic algorithm requires performing $(M+N)N$ one-dimensional DFTs, while a monochromatic algorithm requires performing $(M+N)$ DFTs. Hence, chromatic algorithm requires a calculation time that is N times longer than that required for a monochromatic algorithm; for example $N = 2048$ for our setup. Furthermore, for a typical semiconductor light source employed in OCT, i.e. with a bandwidth of a few tens of nanometers, we could not observe any significant differences in the qualities of the OCT images of monochromatic and chromatic algorithms. Hence, it is more reasonable to use the monochromatic algorithm than the chromatic algorithm.

#9985 - $15.00 USD Received 15 December 2005; revised 20 January 2006; accepted 23 January 2006

4.4. One-dimensional and two-dimensional deconvolution

Another implicit approximation employed in this method concerns the order of the spatial dimension of the deconvolution filter. In this deconvolution method, both the lateral structures of the sample and the probe field are regarded as one-dimensional functions of the lateral position x, whereas, in reality, both of them are lateral two-dimensional functions. Consequently, the designed deconvolution filter is also a one-dimensional function of x.

In principle, it is a straight forward task to design a two-dimensional deconvolution filter and obtain a three-dimensional dataset (a volume scan) by using an additional lateral mechanical scan [12,18–20]. However, in practice, the phase of the volume scan is no longer stable because the scanning time for the volume scan is relatively more than that of for a B-scan. For example, in our setup, the standard deviation of phase within a single B-scan, which contains 512 A-scans, is 2.3 degrees, whereas that of a volume scan, which contains 256 B-scans, is 27.1 degrees. Since the deconvolution method relies on the phase of the OCT signal, the instability in the phase of the volume scan hampers the deconvolution via this method. The reconstructed image quality with a two-dimensional deconvolution filter is not as good as that with a one-dimensional filter, hence it is reasonable to use a one-dimensional filter.

5. Conclusions

In conclusions, we presented a numerical lateral deconvolution method to cancel the defocusing in OCT images. This method uses a depth-dependent lateral point spread function of OCT, and some approximations were introduced in order to design a deconvolution filter. The improved lateral resolution achieved by using this filter was theoretically estimated, and it was shown that in the OOF region, the improved resolution is twice better than the transform-limited resolution (superresolution). The effect of superresolution has also been confirmed experimentally by a razor blade test. In this test, it was shown that this method enhances the SNR of an OCT image. This method was applied to OCT images of *in vivo* human anterior eye segments, and it cancels the defocusing in these images.

The maximum allowable NA of the objective to demonstrate the effect of superresolution was theoretically estimated as 0.11 for our experimental setup. The effect of superresolution is evident only in the OOF range and it has been implied theoretically and confirmed experimentally. The possibilities of chromatic and two-dimensional extensions of this method were discussed. These discussions suggest that monochromatic and one-dimensional algorithm is reasonable for use in practical applications.

Appendix

A. Fourier transform of lateral point spread function

To obtain Eq. (9), the lateral point spread function of FD-OCT described by Eq. (8) is Fourier transformed. Here we describe the details of the Fourier transform.

With definitions of $a \equiv \alpha\lambda^2 f^2 / \left(\alpha^2\lambda^4 f^4 + \lambda^2 z_0^2\right)$ and $b \equiv 2\lambda z_0 / \left(\alpha^2\lambda^4 f^4 + \lambda^2 z_0^2\right)$, Eq. (8) is rewritten as

$$h(x) = \exp\left(-\pi a x^2\right) \exp\left(i\pi b x^2\right) \equiv \exp\left(-\sigma x^2\right) \tag{19}$$

where $\sigma = \pi(a - ib)$, and $h(x, z_0)$ is denoted as $h(x)$ for simplicity.

#9985 - $15.00 USD Received 15 December 2005; revised 20 January 2006; accepted 23 January 2006

The Fourier transform of $h(x)$ is

$$H(\xi) = \int_{-\infty}^{\infty} \exp\left(-\sigma x^2\right) \exp\left(-i2\pi\xi x\right) dx$$
$$= \int_{-\infty}^{\infty} \exp\left\{-\sigma\left(x+\frac{\rho}{2}\right)^2 + \frac{\sigma\rho^2}{4}\right\} dx$$
$$= \exp\left(\frac{\sigma\rho^2}{4}\right) \int_{-\infty}^{\infty} \exp\left\{-\sigma\left(x+\frac{\rho}{2}\right)^2\right\} dx \quad (20)$$

where $\rho = i2\pi\xi/\sigma$.

In general, the integration of Gaussian function is

$$\int_{-\infty}^{\infty} \exp\left(-\frac{x^2}{\beta}\right) dx = \sqrt{\pi\beta}. \quad (21)$$

By using this integration, $H(\xi)$ becomes

$$H(\xi) = \sqrt{\frac{\pi}{\sigma}} \exp\left(\frac{\sigma\rho^2}{4}\right) = \sqrt{\frac{1}{a-ib}} \exp\left(-\pi\frac{1}{a-ib}\xi^2\right)$$
$$= \sqrt{\frac{1}{a-ib}} \exp\left(-\pi\frac{a}{a^2+b^2}\xi^2\right) \exp\left(-i\pi\frac{b}{a^2+b^2}\xi^2\right). \quad (22)$$

Finally, the inverse of the Fourier transform of Eq. (8) is given as

$$H^{-1}(\xi) = \sqrt{a-ib}\, \exp\left(\pi\frac{a}{a^2+b^2}\xi^2\right) \exp\left(i\pi\frac{b}{a^2+b^2}\xi^2\right). \quad (23)$$

B. Phase property of $H^{-1}(\xi)$

To obtain the deconvolution filter of Eq. (12), we set the amplitude of Eq. (9) to 1. To validate this setting for any ξ, a and b in Eq. (9) should fulfill the following conditions; $a \ll 1$ and $a \ll b$.

Under the condition of $a \ll b$, the phase of Eq. (9) becomes

$$\pi\frac{b}{a^2+b^2} = \frac{\pi}{b} = \pi\left(\frac{\alpha^2\lambda^4 f^4 + \lambda^2 z_0^2}{2\lambda z_0}\right) = \pi\left(\frac{\alpha^2\lambda^4 f^4}{2\lambda z_0} + \frac{\lambda^2 z_0}{2\lambda}\right). \quad (24)$$

The second term of the right-hand-side of this equation tends to infinity when $z_0 \to 0$.

The approximation of Eq. (10) is introduced to eliminates this singularity.

Acknowledgements

We would like to acknowledge technical contributions from Takashi Endo, Masahiro Yamanari and Gouki Aoki. Helpful discussions from Dr. Masahiro Akiba of Yamagata Promotional Organization for Industrial Technology and a challenging question from Dr. Tadao Tsuruta of Nikon Corporation in a conference are also gratefully acknowledged. This research is partially supported by the Grant-in-aid for Scientific Research 15760026 from the Japan Society for the Promotion of Science (JSPS), Japan Science and Technology Agency, and the Special Research Project of Nanoscience at University of Tsukuba. Shuichi Makita is supported by JSPS through a contract under the Promotion of Creative Interdisciplinary Materials Science for Novel Functions, 21st Century Center of Excellence (COE) Program.